International Journal of GEOMATE, Oct., 2025 Vol.29, Issue 134, pp.159-168
ISSN: 2186-2982 (P), 2186-2990 (O), Japan, DOI: https://doi.org/10.21660/2025.134.5156
Geotechnique, Construction Materials and Environment

ANALYSIS OF THE CAUSES OF DEFORMATION AND FAILURE OF TRACTION-TYPE SLOPES: A CASE STUDY OF SLOPE ON TIANXI HIGHWAY IN GUANGXI, CHINA

Xiu Xue[1,2], * Mastura Azmi[1]

[1]School of Civil Engineering, Universiti Sains Malaysia, Engineering Campus, Nibong Tebal, 14300 Malaysia;
[2]School of Civil and Engineering, Nanning University, China

*Corresponding authors: Received: 25 July 2025, Revised: 25 Aug. 2025, Accepted: 26 Aug. 2025

ABSTRACT: Slope deformation poses a severe challenge to highway construction. To explore the failure mechanism of typical traction-type deformation slopes, this study systematically evaluated the deformation mechanism of the right slope of the K170+080~K170+260 section of the Guangxi Tianlin to Xilin Highway (referred to as Tianxi Highway) based on field survey and monitoring data, combined with the finite element software PLAXIS 2D. The results show that the sliding zone of the slope is buried at a depth of about 16 m, mainly composed of strongly weathered sandstone, with a semi-soil structure and poor permeability. It is easy to soften under rainfall or surface water infiltration conditions, forming a weak structural surface. The earliest deformation of the slope occurred on June 14, 2021, and then it continued to slide slowly. The toe of the slope was destroyed first, and the upper part suffered delayed destruction about 5 months later. The sliding surface was finally connected, showing typical traction-type deformation characteristics. It shows that the landslide starts from the lower part of the slope, and the toe support should be given priority in reinforcement and management. The internal causes of landslides are mainly special landforms and complex rock and soil structures, while the external causes include artificial excavation and heavy rainfall. Among them, although the excavation work caused some disturbance, the unreasonable drainage layout and the long construction period led to a large amount of rainwater infiltration, which became the main triggering factor. Therefore, the focus of governance should be on improving the drainage system to reduce the impact of rainfall infiltration. This study reveals the progressive deformation mechanism of the typical traction slope of Tianxi Highway under the combined effects of complex geology and rainfall-excavation, clarifies the characteristics of the sliding surface and the main causes, and has important reference value for similar slope stability analysis and engineering prevention and control.

Keywords: Traction-type slope, Weak interlayer, Excavation, Rainfall, Formation Mechanism.

1. INTRODUCTION

Landslides are frequent and highly destructive geological disasters. For example, in January 2022, a landslide occurred at a construction site in Bijie City, Guizhou Province, China, killing 14 people and injuring 3 people [1]. On October 5, 2021, a landslide and mudslide disaster chain occurred in Hanping Village, Shanxi Province. This major disaster chain destroyed 7 houses, 41.9 hectares of cultivated land, 3 roads, and caused 1 death [2]. In August 2017, a major landslide occurred in a mining area in Bijie City, Guizhou Province, China, dumping 82,3000 m3 of rubble and causing heavy casualties [3]. There are many cases of economic losses and casualties caused by such landslides, so it is particularly important to explore the mechanism of landslide deformation. This is not only a need for landslide control, but also provides a reference for future landslide warnings and emergency measures after disasters.

At present, domestic and foreign scholars have also done a lot of analysis and research on landslide deformation. Xi et al. used FLAC3D finite element software combined with indoor rainfall tests and on-site ecological protection tests to analyze the cutting slope landslide mechanism in the K28 section of Shuangda Highway in Gansu Province, and proposed corresponding ecological prevention and control measures [4]. Liu et al. used the DS-InSAR method to find that the deformation characteristics of the landslide area are jointly affected by factors such as geological structure, rainfall and slope angle [5]. Miao et al., through mining and analysis of monitoring statistical data, found that the deformation of the Baishuihe landslide in the Three Gorges Reservoir area is highly correlated with accumulated rainfall. The daily rainfall threshold is a critical value of 73.9mm. After this value is exceeded, landslide activity becomes apparent accelerated [6]. Based on block theory, Sun et al. used GDEM finite element software to study the stability and dynamic response of dangerous rock masses under self-weight conditions and seismic loads, and provided suggestions about targeted prevention, monitoring and early warning methods[7]. Li et al. took a highway landslide in southwest China as an example [8]. Based on contracts in blockchain technology to analyze 3D monitoring data to explore the initiation mechanism geological survey and investigation, they used smart of the landslide. Xie et al. took the

dangerous rock mass on the right side of Yuanhou Toll Station on Rongzun Highway as the research object, used drone technology to establish a deformation and failure model, and used FLAC3D and Rockfall software to find that the stress concentration of the dangerous rock mass in the middle and lower soft rocks was relatively large, and there was a 60% probability of failure once the rockfall collapsed [9]. Sun et al. focused on the multiple influences of geological structure, rock and soil properties, groundwater and external triggering factors (such as rainfall or earthquake) on the deformation and failure mechanism of the landslide through field investigation, indoor experiments and numerical simulation [10]. And these factors have a dominant control effect on the stability of the landslide. Hou et al. used field investigation, indoor experiments, mineral identification, in-situ monitoring, finite element simulation and other methods to explore the formation mechanism and stability of the expansive soil landslide in the Three Gorges Reservoir area of China [11]. Hu et al. conducted model experiments and analyzed 675 sets of test data, and found that the main deformation mode of long and long bedding slopes is sliding deformation, the failure mode is sliding-crack failure, and the sliding process is graded sliding [12]. Rotaru et al. used geological and mechanical principles and combined with dynamic monitoring data to analyze the occurrence mechanism, dynamic characteristics and movement laws of landslides in detail, revealing the complexity of landslide triggering and the influence of moisture, geological conditions and external disturbances on landslide activity [13].

In summary, most slope deformation is analyzed and studied based on field investigation, drilling, geophysical exploration, aerial photography, in-situ monitoring etc., with the help of numerical simulation, data analysis and other means. The results show that excavation, rainfall, earthquakes, etc. are the main external factors that induce slope deformation and instability. In addition, some internal factors such as the special lithological characteristics and geological structure (joints and fissures) of the slope itself are also important causes of slope failure and deformation. This paper takes the right-side slope of the K170+080~K170+260 section of the Tianxi Highway as an example, and uses geological exploration, indoor experiments, in-situ monitoring, numerical simulation and other methods to explore its deformation characteristics, evolution process and cause mechanism, providing a reference for the investigation and early warning of the same type of slopes.

To overcome the common decoupling of investigation, monitoring, and numerical analysis under excavation–rainfall coupling, we develop an integrated chain of evidence for the K170 right-side slope. Field observations and PLAXIS 2D back-analyses are used to constrain the geometry and materials of the sliding surface and to evaluate how rainfall infiltration, drainage conditions, and excavation jointly govern traction-type evolution. The objectives are to (i) clarify the progressive deformation mechanism, (ii) assess the influence of drainage deficiencies, and (iii) derive stabilization implications.

2. RESEARCH SIGNIFICANCE

This study makes a novel contribution by establishing a chain of evidence linking field monitoring and PLAXIS 2D analyses to reveal progressive deformation in traction-type slopes. Departing from single-factor interpretations, we quantify the coupled impacts of rainfall infiltration, excavation disturbance, and rock–soil heterogeneity on instability. Constraining the sliding surface's depth, composition, and delayed-failure sequence yields a mechanistic picture of traction-type evolution. Evidence indicates that drainage-system deficiencies act as the principal trigger during rainfall, converting mechanism to practice through priorities of toe buttressing and surface–subsurface drainage. These insights provide transferable guidance for prevention, design, and early warning of similar highway slopes.

3. PROJECT OVERVIEW

3.1 Topography and Geological Structure

The site is a hilly landform unit with a height difference of about 80m and a span of 190m along the roadbed. The overlying soil layer is clay from the residual slope accumulation layer of the Quaternary System, and the bedrock is sandstone from the Lanmu Formation of the Middle Triassic System. The mountain slope is 45°~60°, the slope height is about 80m, the surface vegetation is well developed, and the landform type is single (Fig. 1). The rock fissures in the landslide area are well developed, the rock mass is relatively broken, and there are no adverse geological disasters such as deformed slopes and collapses in the area. The regional geology is stable. The rock formations in the survey area were measured to have undulating dips. The dip of the rock formations at the foot of the slope is $70°\angle 45°$, tending to the inside of the slope, and the dip of the rock formations of grades 2~4 on the slope is 203° $\angle 56°$, tending to the outside of the slope. Two groups of dominant joints were also measured: J1: $110°\angle 55°$ (7 joints/m), J2: $130°\angle 85°$ (3 joints/m). Stereonet-based kinematic analysis indicates that in the mid–upper slope the bedding (203°∠56°) is subparallel to the slope aspect; where local slope angles $\beta \geq 57°$, the daylighting criterion is satisfied [$\alpha(=56°) < \beta$], and because $\alpha > \varphi$, bedding-

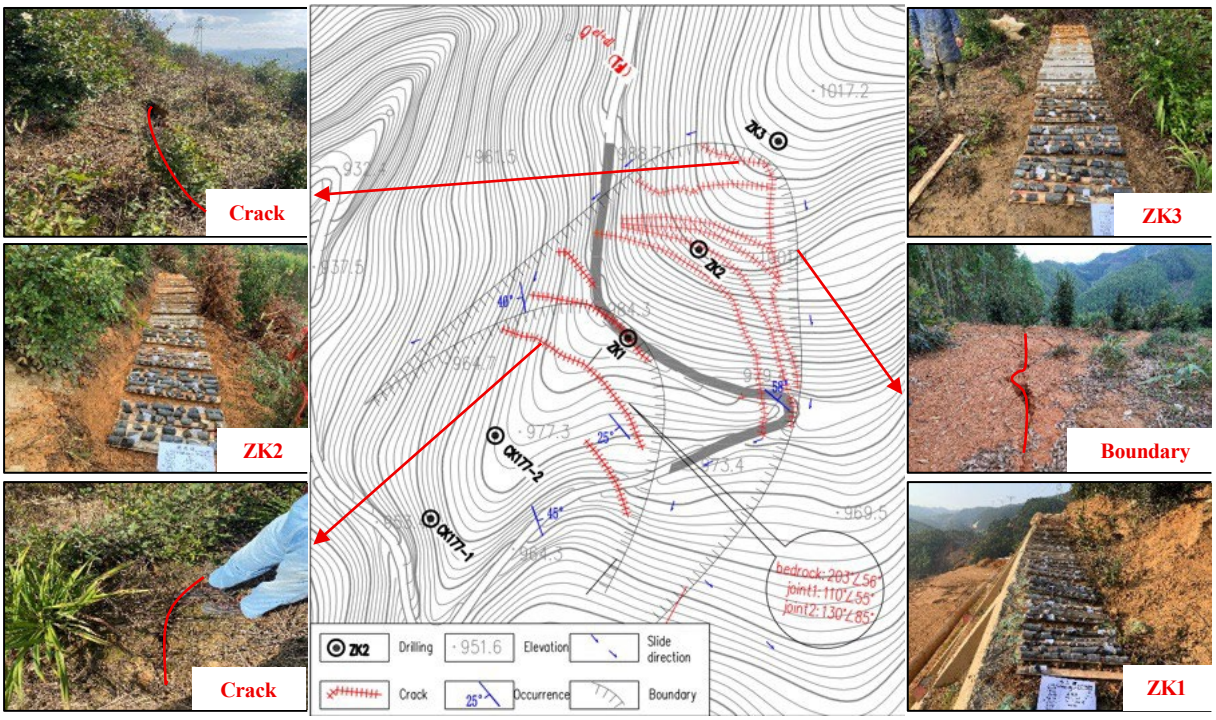

Fig. 1. Engineering geological plan of project area and photo

parallel tractional (translational) sliding is kinematically feasible. In contrast, the toe bedding (70°∠ 45°) dips into the slope and does not daylight, providing some confinement. The joint sets are oblique to the slope strike, so wedge and toppling modes are not favored. Overall, tractional deformation/failure is most likely to localize within the steeper mid–upper segments.

3.2 Formation lithology

Within the scope of the survey depth, the site strata are divided from top to bottom into the Quaternary residual slope accumulation layer (Q^{el+dl}) and the Lanmu Formation (T_2l) of the Middle Triassic System according to the stratigraphic age, genesis, lithology, physical and mechanical properties.

Quaternary eluvial–colluvial deposits (Q^{el+dl}). Predominantly silty clay, locally containing fragments of weathered sandstone; yellowish-red to yellow in color; heterogeneous; of stiff-plastic consistency with moderate dry strength and tenacity. This unit is mainly distributed in the shallow part of the slope and was encountered in boreholes ZK2, ZK3, and ZK4. Its regional thickness generally ranges from 4.0 to 10.0 m.

The Lanmu Formation (T_2l) of the Middle Triassic System is mainly sandstone, with mudstone in some parts. According to geological survey and drilling data, the rock can be divided into two layers: strongly weathered and moderately weathered, according to the degree of rock weathering, as described below:

Strongly weathered sandstone, grayish yellow, yellowish brown, fine-grained structure, medium-thick layered structure, soft rock, interbedded with strongly weathered mudstone. The rock mass is broken, joints and fissures are developed, the fissure surface is infected with iron and manganese, and contains mud cementation. The rock mass is relatively soft, and the upper part is unevenly weathered. The core is mostly in the form of debris blocks and sandy soil. A small amount is short columnar, with a block diameter of 1 to 6 cm, and the drilling is slightly faster. This layer is revealed in all the drill holes in the site, with a thickness of 15.6m.

Moderately weathered sandstone, gray, gray-black, fine-grained structure, medium-thick layered structure, hard rock, relatively complete rock mass, partially interbedded with mudstone, the core is columnar, short columnar, and the drilling is stable. This layer is revealed in all the drill holes, with a maximum revealed thickness of 29.7m, and it has not been drilled through.

3.3 Meteorology and Hydrology

The site is in western Guangxi, and the entire area has a subtropical continental monsoon climate. There is sufficient light and heat, no severe cold in winter, and no scorching heat in summer. The distribution of annual precipitation has obvious seasonal characteristics. May to August is the rainy season, with frequent heavy rains, and the precipitation accounts for two-thirds of the total annual amount.

The groundwater in the borehole depth is mainly fissure water in the strongly and moderately

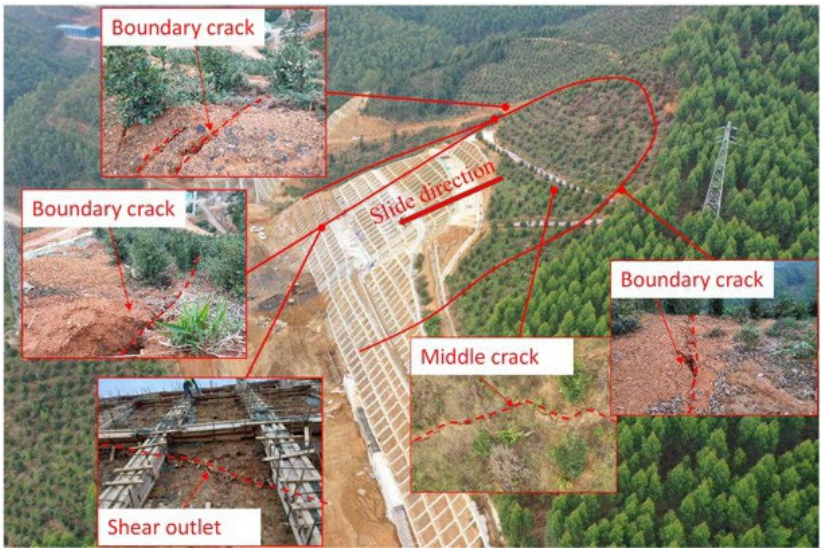

Fig.2. Landslide deformation site photos

weathered sandstone. The main source of fissure water recharge is atmospheric rainfall, which infiltrates the ground and discharges vertically into the ground along the fissure runoff. The amount of water varies greatly depending on the degree of development of rock fissures. The dynamics of groundwater are significantly affected by atmospheric precipitation and surface water dynamics, and the annual fluctuation of water level is large.

4. SLOPE DEFORMATION CHARACTERISTICS

4.1 Characteristics of Slope Surface Failure

On November 27, 2021, the slope deformed and damaged. The main sliding direction of the deformed slope was 220°, the longitudinal length was about 150m, the lateral width was about 130m, the height difference was about 25m, the area was about $2.0\times10^4m^2$, the sliding body thickness was about 2.0~16m, and the volume was about $8.0\times10^4m^3$. It is a large traction-type deformed slope.

The front edge of the deformed slope is cut out and is located at the bottom of the second-level slope. The lowest elevation of the front edge is about 950m; the rear edge elevation is about 1020m, located 40 to 70m above the top of the original designed slope. Cracks of varying degrees occur at the rear edge of the slope at a position of 5 to 20m. The cracks are in the shape of a round chair, with crack widths ranging from 5 to 100cm and a maximum visible depth of 60cm. As time goes by, the cracks at the rear edge further develop, with the farthest crack being about 76m from the slope opening line, and the cracks continue to develop and penetrate, forming a round chair shape. The on-site photo is shown in Fig.2.

4.2 Characteristics of Deep Deformation and Failure

Two inclinometer boreholes were installed along the K170+130 slope section to monitor its deformation process. Borehole ZK1 (elevation 982.0 m), located at the middle of the slope, served as inclinometer K170+130-1, while another inclinometer, K170+130-2 (elevation 959.1 m), was placed further downslope.According to the monitoring data, as shown in Figure 3, the cumulative displacement at K170+130-1 began to accelerate significantly from June 17 to July 3, 2021, reaching 30.57 mm. Displacement continued over the following two months, ultimately reaching a maximum cumulative value of 144.72 mm by early September. A pronounced inflection point around an elevation of 963.4 m marks the location of the sliding surface, estimated at approximately 16 m below the slope surface. Beyond this point, a sudden drop in data indicates shear-induced destruction of the inclinometer due to slope failure.

In contrast, K170+130-2 (Figure 4) recorded earlier deformation, with measurable outward movement beginning on June 14, 2021. Cumulative displacement increased over the next three days, with the instrument ceasing to function after June 17, again attributed to shear damage near the sliding zone at approximately 941.1 m elevation. The comparison of these two profiles reveals that the lower part of the slope deformed earlier than the upper, confirming the presence of a progressive, traction-type failure mechanism, where initial movement originates from the lower slope and propagates upward. By November 27, 2021, displacement had accumulated to the point where the failure surface fully penetrated the slope body, resulting in large-scale shearing and

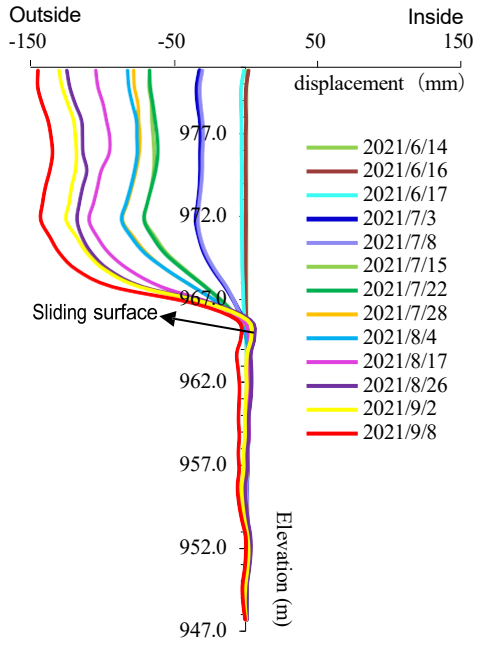

Fig.3. K170+130-1 Cumulative displacement

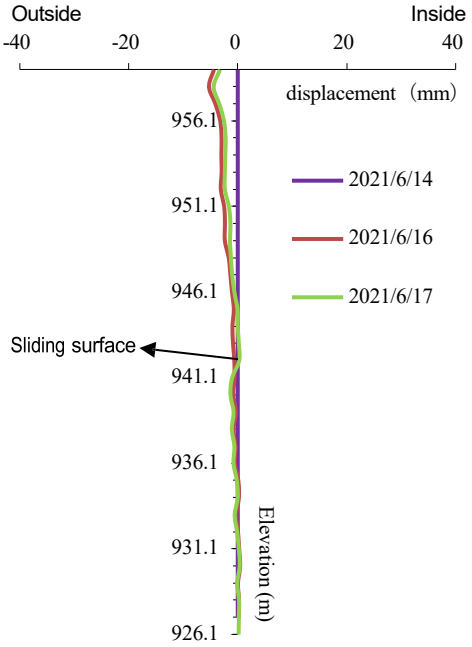

Fig.4. K170+130-2 Cumulative displacement

overall slope destabilization. In this deformation section, the surficial cover consists of Quaternary eluvial–colluvial silty clay with a measured thickness of 5.0–9.4 m; it is underlain by 15–23 m of strongly weathered sandstone. The sliding zone is situated within a weak structural interface of highly weathered sandstone, characterized by gravelly and blocky textures with irregular fractures. The upper slope materials, being semi-consolidated and of low permeability, further facilitated pore pressure accumulation during rainfall events, ultimately triggering and accelerating the failure process.

5. CAUSE ANALYSIS

5.1 Topography and Adverse geology

The site is a denuded mid-mountain landform with steep surface slopes and well-developed gullies between mountains. The surface vegetation is well-developed, with sugar oranges planted in the middle and upper parts of the slope, and a 500KV high-voltage line tower at the back edge of the slope. The slope is about 190m long and 80m high, with large terrain fluctuations. The slope surface angle is generally between 45° and 65°, and the slope is steep in some areas. The terrain conditions are not conducive to slope stability. In addition, the geological structure of the slope is well-developed, joints and fissures are well-developed, and the rock mass is broken. At the same time, continuous joint surfaces are easily formed, creating relatively good objective conditions for groundwater infiltration.

5.2 Geotechnical Structure

Based on drilling exposures combined with cumulative displacements from deep inclinometers, the deforming mass consists of Quaternary residual–colluvial silty clay overlying strongly weathered sandstone. The weathered zone is thick and structurally loose, with poor erosion resistance and pronounced water-softening, making the assemblage prone to sliding and other adverse geological effects under rainfall infiltration. Notably, the internal sliding zone, together with poorly permeable soil layers, forms a relatively impermeable horizon (relative aquitard). Infiltration along this interface leads to softening and weakening in and around the boundary, thereby developing a softened shear band. This band markedly reduces the mechanical strength and exerts a controlling influence on overall stability; the slip surface aligns with this weak zone and governs the deformation–failure mode. Owing to the damaged front inclinometer borehole, uncertainties persist in the basal slip surface's depth/continuity, necessitating verification drilling to obtain direct constraints on its geometry and parameter evolution.

5.3 Rainfall

As shown in Fig. 5, the slope experienced sustained heavy rainfall after excavation; the daily total reached 26 mm on 17 November, followed by overall sliding. To quantify the rain–rate relationship, we used site daily rainfall and the inclinometer daily displacement rate, and constructed the same-day antecedent five-day rainfall $!"_!(\$) = \sum_{\&\&}^{\%} \cdot ("_{\#\$}$. We performed paired analyses only when both daily displacement rate and AR5(t) were available on the same day (Fig. 6), yielding three pairs on 26 Aug, 2

Sep, and 8 Sep. Figure 1 shows that after the small-to-moderate rain on 24–25 Aug (3.25 and 2.80 mm), the rate on 26 Aug was the highest among the three observations; 2 Sep was lower, and 8 Sep was near zero. The regression indicates +0.0059 mm·d^{-1} per 10 mm of AR5(t), but the 95% CI spans zero, implying that the effect size is uncertain under the current sample size.

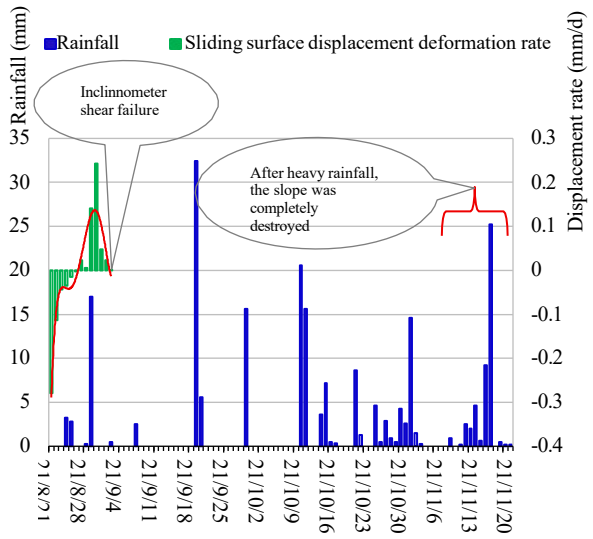

Fig.5. Rainfall and landslide displacement deformation rate diagram

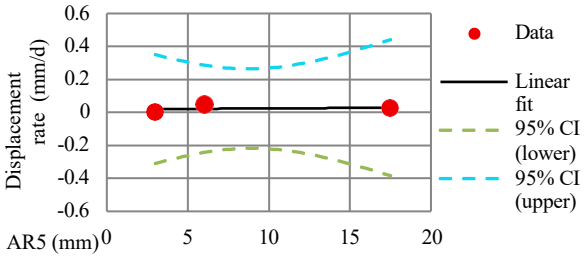

Fig.6. Rainfall and landslide displacement deformation rate diagram

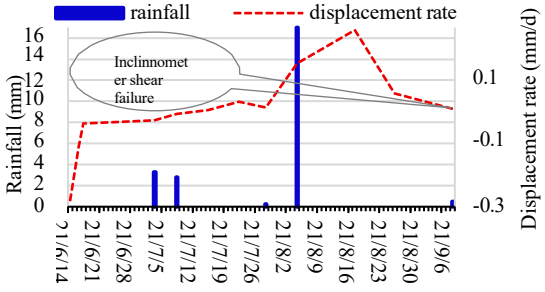

Fig.7. Rainfall and landslide displacement deformation rate diagram

Figure 7 suggests a monotonic tendency of increasing displacement rate with larger short-term antecedent rainfall, consistent with the mechanism whereby infiltration along weak interlayers reduces shear strength and increases unit weight, promoting slip. However, because the inclinometer failed on 8 Sep, no subsequent rate data are available; thus, although the mid-November storm coincides with the failure timing, the results should be regarded as indicative of direction and magnitude only.

5.4 Human Activities

According to the construction time trajectory and the preliminary survey data, the slope did not show any signs of deformation in the preliminary survey. The deformation of the slope mainly occurred shortly after the excavation, and the slope foot had not yet been supported before the collapse occurred. This is because the excavation will cause the slope stress to be transferred to the upper part, forming a stress concentration area. In addition, the unloading process of the slope excavation will cause the stress to be released, and the deformation will be further aggravated. Besides, the slope construction took a long time and the platform intercepting ditch was not constructed in a standardized manner (Fig. 8), which also caused rainwater to infiltrate the slope along the ditch.

Fig. 8 Inadequate drainage facilities

6. DEFORMATION MECHANISM ANALYSIS

6.1 Model Building

To study the deformation process of the slope, PLAXIS2D software was used to simulate and perform two-dimensional finite element analysis. According to the profile and related drilling data, a model as shown in Figure 9 was established, which is 200m long and 73m high. The model is divided into 1042 units and 8513 units nodes. This paper adopts a baseline Mohr–Coulomb model within a fully coupled seepage–deformation framework, using Bishop's effective stress and SWCC-based saturation updates to unify the representation of excavation-induced stress redistribution and rainfall-driven pore-pressure/suction evolution, thereby elucidating their governing influence on slope deformation.

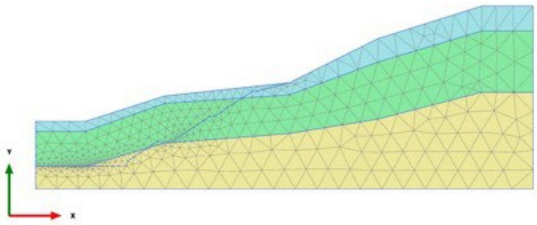

Fig.9. Numerical analysis model of PLAXIS2D

Rationale for Table 1 parameter selection: initial physical and strength values were established via reconnaissance–sampling–laboratory testing(Direct shear, etc.); c′–φ′ were inversely determined, within bounded ranges, under the code-based saturated limit state (K=1.00) using the transfer-coefficient method and forward-checked against displacement time histories and slip-surface depth under natural/saturated conditions; ν and E were taken from soil-type empirical ranges and verified in the same manner; k was inversely obtained by matching the phreatic surface and toe seepage with SWCC shape parameters held fixed; all final values fall within laboratory results and literature envelopes for comparable soils[14-19].

Table 1 Physical and mechanical parameters of rock and soil

Layer	unit weight/kN·m^{-3}		E	ν	c	φ	k
	Natural	Saturated					
1	18.5	19.5	12	0.3	14	20	1.7×10^{-7}
2	23.5	24.5	15	0.25	18	22	5.6×10^{-8}
3	25	26	50	0.25	20	40	2.2×10^{-8}

Note:1-Q^{el+dl}, 2-T_2l (upper), 3-T_2l (lower), E-Elastic modulus (MPa), ν-Poisson's ratio, c- Cohesion (kPa), φ-Internal friction angle (°), k- Permeability coefficient ($m\cdot s^{-1}$).

The hydraulic boundary conditions were specified as follows: the left and right boundaries were treated as free-seepage boundaries permitting lateral drainage, and the base was set as impermeable. The initial water table was assigned according to the groundwater depth determined from the site investigation. A rainfall-flux boundary was applied on the ground surface; when positive pore-water pressure developed at surface elements, the boundary automatically switched to a seepage face. To capture the short-term effect of rainfall on slope response, a daily rainfall of 60 mm was adopted (2.5 mm/h), based on multi-year statistics for Xilin County that represent typical wet-season heavy-rain events and consistent with the Chinese operational definition of a "rainstorm" (24h ≥ 50mm); this choice is representative yet conservative for the region.

The factor of safety (FS) is computed using the shear strength reduction (SSR) method: without seepage, the prescribed pore-water pressure is used, and after staged excavation the model enters the Safety phase, where c′ and tan φ′ are simultaneously reduced by a uniform strength-reduction factor (SRF) until incipient failure; the critical SRF* is taken as FS. With seepage, a fully coupled seepage–deformation analysis is first run to the target time to obtain the pore-pressure, which are then frozen; the same SSR procedure is applied in the Safety phase by reducing c′ and tan φ′ to failure, yielding FS for that time slice. Unsaturated effects are incorporated via Bishop's effective stress with saturation derived from the SWCC.

6.2 Deformation Mechanism Analysis

Initial field investigations indicated that the slope was stable under natural conditions. However, deformation developed following excavation associated with highway construction. Numerous statistical studies [20–22] have shown that both natural and engineered slopes commonly fail during or shortly after rainfall, particularly in infrastructure settings such as highways, railways, and open-pit mines.

Figure 10 compares deformation and stability responses under four boundary conditions: natural state, rainfall only, excavation only, and excavation + rainfall. As shown in Fig. 10a, the slope is overall stable in the initial state (FS = 2.100); displacement increments are minor, appearing only as a faint band along the upper slope surface and the shallow part of the potential slip surface, reflecting slight downslope movement under self-weight, while toe support remains evident. After rainfall is applied (Fig. 10b), infiltration causes matric-suction dissipation and pore-pressure rise; the high–displacement-increment band extends and intensifies along the mid- to upper slope, but because the toe has not been weakened, the deep band remains shallow. The FS drops to 1.478 yet remains above critical, indicating a rainfall-dominated triggering effect. Under excavation alone (Fig. 10c), the cut weakens toe support and redistributes stresses; relative to Fig. 10a, the high–displacement-increment band thickens and connects downward to the cut surface, with a concentrated zone at the toe–cut interface. The FS is 1.559, showing that the geometric weakening induced by excavation has placed the slope in a preconditioned weakened state. When 24 h of rainfall is superimposed on the excavated slope (Fig. 10d), the displacement-increment band becomes continuous, thickens, and links from the mid-upper slope down to the toe; both peak magnitude and areal extent increase markedly, with the strongest response near the potential slip surface. The FS further decreases to 1.153, exhibiting traction-type upward propagation and revealing the coupled deterioration process of excavation preconditioning together with cumulative weakening due to rainfall infiltration.

Figure 11 examines, with the post-excavation geometry and boundaries held fixed, how different rainfall durations (0, 12, and 36 h) affect the matric

suction field and stability. At 0 h (Fig. 11a), the slope maintains high matric suction overall, with only sporadic low-suction pockets at the near surface and the toe; the wetting front has not yet formed (FS=1.559). At 12 h (Fig. 11b), suction decreases markedly along the near-surface and upper slope, developing a continuous shallow low-suction band along the slope face; suction also drops near local weak zones and becomes connected with the cut surface (FS=1.213). By 36 h (Fig. 11c), the low-suction zone thickens and migrates downward; suction isolines advance deeper and become denser, and the low-suction extent expands into the middle ─ lower slope and the toe, concentrating near the potential slip surface (FS=1.133).

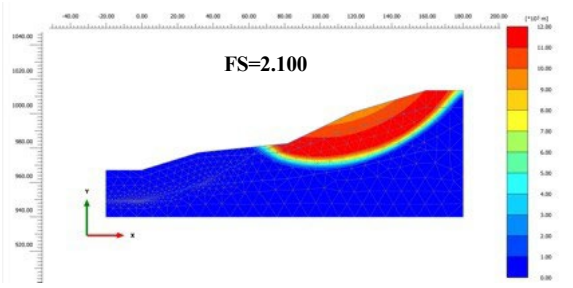

(a) Initial state

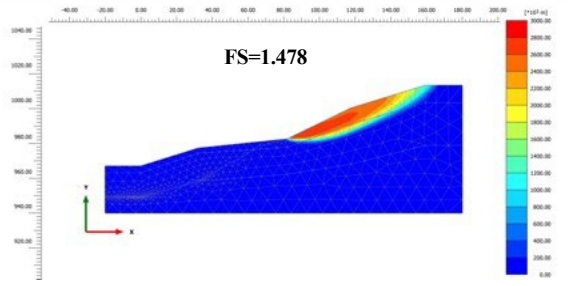

(b) Original state + Rainfall

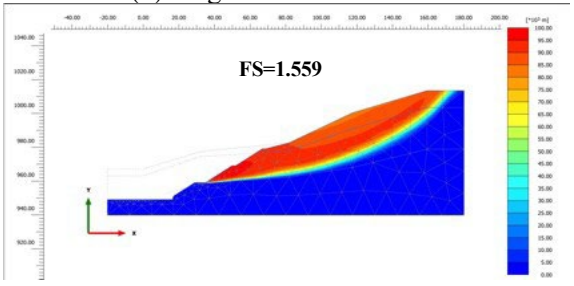

(c) Excavation

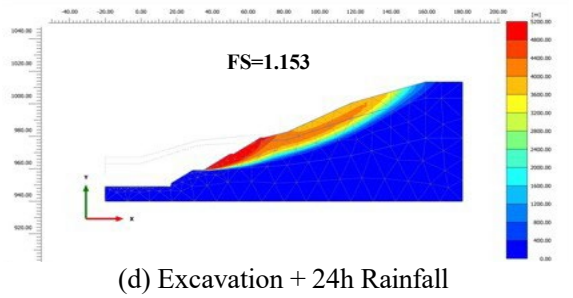

(d) Excavation + 24h Rainfall

Fig. 10 Displacement increments cloud diagram under different working conditions

Stability degradation follows a monotonic pathway governed by rainfall duration, from suction dissipation to effective-stress reduction and strength loss; this accords with the coupled mechanism of excavation and cumulative weakening due to prolonged infiltration, accounting for the observed temporal decrease in stability.

These results indicate that excavation preconditions the slope by weakening toe resistance and concentrating deformation, while subsequent rainfall infiltration dissipates matric suction and elevates pore-water pressure, thereby triggering and amplifying shear deformation. Failure propagates upward from the toe, exhibiting a typical traction-type evolutionary path. The spatial position and evolution trend of the potential slip surface are consistent with monitored deformation data, supporting the fidelity of the numerical model.

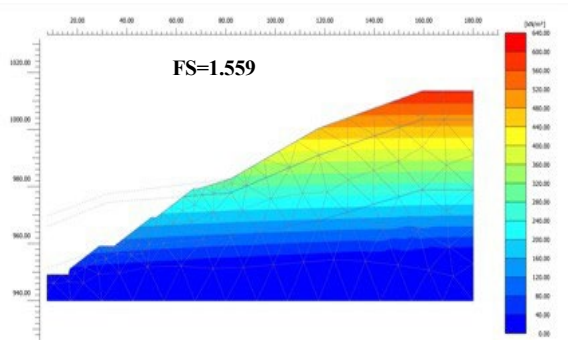

(a) Excavation + 0h Rainfall

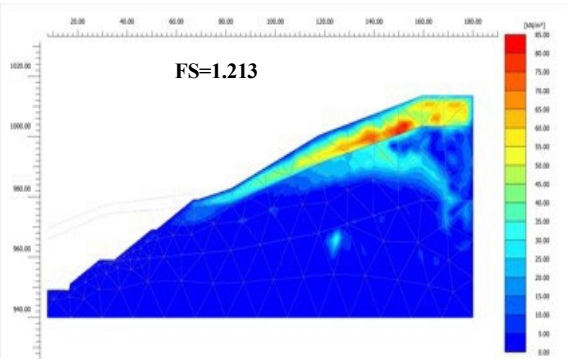

(b) Excavation + 12h Rainfall

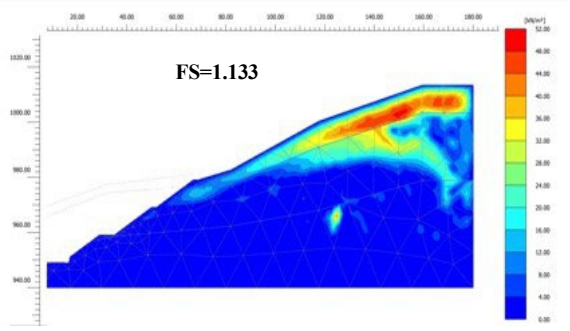

(c) Excavation + 36h Rainfall

Fig. 11 Matrix suction cloud map under different rainfall conditions

7. DISCUSSION

Field evidence and modeling indicate a traction-type progressive failure: instability initiated at the toe and subsequently pulled the upper slope into motion, producing a front-to-rear enlargement of the failure zone that departs from classical shear- or push-type landslides. Although excavation caused localized stress redistribution, its effect was largely constrained by existing toe support; by contrast, rainfall infiltration was decisive. PLAXIS 2D results under rainfall reproduce the observed loss of stability and upslope migration of plasticity, consistent with monitoring. Geologically, a weakly permeable interlayer over strongly weathered sandstone focuses wetting, suction dissipation, and softening, thereby organizing the mechanical sliding band—highlighting the controlling role of internal weak zones often under-recognized in conventional assessments.

The numerical analysis in this study is mechanism-oriented rather than event-reconstructive. (i) Model framework & boundaries: PLAXIS 2D adopts a plane-strain scheme with idealized rainfall/hydraulic boundaries and simplified support, thus omitting 3-D drainage, lateral buttressing, and spatial variability. (ii) Material & hydrologic representation: a Mohr–Coulomb law without explicit strain-softening/anisotropy was used; unsaturated-flow functions were constrained by limited site data and do not explicitly represent preferential-flow or fracture networks. (iii) Data limitations: the absence of piezometer/suction observations and the short rainfall record prevent direct validation of transient pore pressures and a robust recurrence analysis. These constraints may bias timing and magnitudes but do not alter the inferred pathway—excavation preconditioning plus rainfall-induced suction loss along weak interlayers. Practically, stabilization should prioritize toe support and drainage and protect/daylighted weak interlayers from infiltration; future work should employ 3-D hydro-mechanical modeling with strain-softening/anisotropy and instrumented monitoring for calibration.

8. CONCLUSION

The sliding zone at the K170 slope is located at a depth of ~16 m at borehole K170+130-1, within strongly weathered sandstone exhibiting a semi-soil fabric and low permeability; infiltration of rainfall and surface water induces softening and weakening, forming a weakened structural interface that controls subsequent deformation and propagation. With the front inclinometer borehole damaged, the depth and geometric continuity of the basal slip surface remain uncertain; verification drilling is required to directly constrain its geometry and the time-dependent evolution of its parameters.

Stereonet-based kinematic analysis indicates that tractional sliding is the dominant mode on the steeper mid–upper slope: the bedding at 203°∠56° becomes susceptible to sliding where the local slope angle $\beta \geq 57°$, whereas the inward-dipping toe bedding (70°∠ 45 °) does not daylight and thus is not prone to sliding. Field monitoring shows that deformation began after June 14, 2021 and migrated upslope over
~5 months, ultimately coalescing into a continuous sliding surface—a hallmark of traction-type failure. Therefore, stabilization should prioritize toe support to interrupt basal sliding and prevent upslope propagation.

Notably, the primary external trigger of slope instability was not excavation activities, but rather the inadequate drainage design and the extended construction period, which allowed large volumes of rainwater to infiltrate the slope. This resulted in increased pore water pressure, reduction in shear strength, and ultimately, landslide initiation. Therefore, improving the design and implementation of surface and subsurface drainage systems is critical for long-term slope stability.

9. ACKNOWLEDGMENTS

This work was supported by the Nanning University School-level Scientific Research Project Funding (2024XJ10).

10. REFERENCES

1. Tao T., Shi W., Liang F., et al. Failure mechanism and evolution of the Jinhaihu landslide in Bijie City, China, on January 3, 2022. Land-slides, Vol. 19, No. 11, 2022, pp. 2727–2736. https://doi.org/10.1007/s10346-022-01957-w
2. Yu Z., Zhan J., Yao Z., et al. Characteristics and mechanism of a catastrophic landslide–debris flow disaster chain triggered by extreme rainfall in Shaanxi, China. Natural Hazards, Vol. 120, No. 8, 2024, pp. 7597–7626. https://doi.org/10.1007/s11069-024-06518-z
3. Xiong S., Shi W., Wang Y., Zhu C., Yu X. Deformation and Failure Process of Slope Caused by Underground Mining: A Case Study of Pusa Collapse in Nayong County, Guizhou Province, China. Geofluids, Vol. 2022, Issue 1, 2022, pp. 1–19. https://doi.org/10.1155/2022/1592703
4. Xi H., Li H., Yan C., et al. Analysis on factors controlling shallow failures of the cut slopes and its prevention by bio-engineering measures: A case study of the cut slopes along the highway from Shuangcheng to Dajiali. The Chinese Journal of Geological Hazard and Control, Vol. 35, No. 3, 2024, pp. 70–79. https://doi.org/10.16031/j.cnki.issn.1003-8035.202211019

5. Liu Y., Yang H., Wang S., Xu L., Peng J. Monitoring and stability analysis of the deformation in the Woda landslide area in Tibet, China by the DS-InSAR method. Remote Sensing, Vol. 14, No. 3, 2022, pp. 1–21. https://doi.org/10.3390/rs14030532
6. Miao F., Wu Y., Li L., et al. Triggering factors and threshold analysis of Baishuihe landslide based on the data mining methods. Natural Hazards, Vol. 105, 2021, pp. 2677–2696. https://doi.org/10.1007/s11069-020-04419-5
7. Sun Q., Ma F., Liu G., Guo J., Duan X. Deformation Failure Mode and Stability Analysis of Kanuna Unstable Rock Mass in the Lhasa–Yangbajing Section of G109 National Highway. Journal of Engineering Geology, Vol. 29, No. 2, 2021, pp. 495–507. https://doi.org/10.13544/j.cnki.jeg.2019-093
8. Li C., Long J., Liu Y., et al. Mechanism analy-sis and partition characteristics of a recent highway landslide in Southwest China based on a 3D multi-point deformation monitoring sys-tem. Landslides, Vol. 18, 2021, pp. 2895–2906. https://doi.org/10.1007/s10346-021-01698-2
9. Xie J., Yang G. L., Qin Y. G., Xu X. T. Deformation Failure Mechanism and Motion Laws of Near-Horizontal Thick-Layer with Thin-Layer Columnar Dangerous Rock Mass in the Chishui Red Bed Area. IOP Conference Series: Earth and Environmental Science, Vol. 570, No. 2, 2020, pp. 1–14. https://doi.org/10.1088/1755-1315/570/2/022045
10. Sun Hy., Wu X., Wang Df., et al. Analysis of deformation mechanism of landslide in complex geological conditions. Bulletin of Engineering Geology and the Environment, Vol. 78, No. 6, 2019, pp. 4311–4323. https://doi.org/10.1007/s10064-018-1406-3
11. Hou T., Xu G., Shen Y., Wu Z., Zhang N., Wang R. Formation mechanism and stability analysis of the Houba expansive soil landslide. Engineering Geology, Vol. 161, 2013, pp. 34–43. https://doi.org/10.1016/j.enggeo.2013.04.010
12. Hu Q., Xie Q., Zheng L. Research on evolvement of the progressive slide and failure mechanism of the long bedding slope. Hydroge-ology & Engineering Geology, Vol. 38, No. 3, 2011, pp. 31–37.
13. Rotaru A., Oajdea D., Răileanu P. Analysis of the landslide movements. International Jour-nal of Geology, Vol. 1, No. 3, 2007, pp. 70–79
14. Schaap M.G., Leij F.J., van Genuchten M.Th. Rosetta: A computer program for esti-mating soil hydraulic parameters with hierar-chical pedotransfer functions. Journal of Hy-drology, Vol. 251, No. 3–4, 2001, pp. 163–176. https://doi.org/10.1016/S0022-1694(01)00466-8
15. Perera Y.Y., Zapata C.E., Houston W.N., Houston S.L. Prediction of the Soil–Water Charac-teristic Curve Based on Grain-Size-Distribution and Index Properties. In: Rathje, E.M. (ed.), Geo-Frontiers 2005 Congress (Geotechnical Special Publications 130–142 & GRI-18), Aus-tin, TX, 24–26 Jan 2005, pp. 49–60. ASCE Geo-Institute & Geosynthetic Materials Association. DOI: 10.1061/40776(155)4.
16. Chin K.-B., Leong E.-C., Rahardjo H. A simplified method to estimate the soil–water characteristic curve. Canadian Geotechnical Journal, Vol. 47, No. 12, 2010, pp. 1382–1400. https://doi.org/10.1139/T10-033
17. Wang S., Guo X., You F., Zhang Z., Shen T., Chen Y., Zhai Q. Estimation of the Soil–Water Characteristic Curve from Index Properties for Sandy Soil in China. Water, Vol. 16, No. 14, 2024, pp. 1–12. https://doi.org/10.3390/w16142044
18. Thota S.K., Cao T.D., Vahedifard F. Poisson's Ratio Characteristic Curve of Unsaturated Soils. Journal of Geotechnical and Geoenvironmental Engineering, Vol. 147, No. 1, 2021, pp. 1–12. https://doi.org/10.1061/(ASCE)GT.1943-5606.0002424
19. Dwinagara B., Akbar W. N., Saptono S., Haryanto D., Haq S. R., Prabandaru P. D., Back Analysis of Rainfall-Induced Waste Dump Failure Using Coupled Hydro-Mechanical Analysis – A Case Study in Coal Mine. International Journal of GEOMATE, 27(123) 2024, pp. 54–64. https://doi.org/10.21660/2024.123.4618
20. Yamashita D., Kanazawa S.-i., Suzuki H., Iida K., Investigation of Stress Behavior in Em-bankment Due to Rainfall Infiltration. Interna-tional Journal of GEOMATE, 26(115) 2024, pp.81–88. https://doi.org/10.21660/2024.115.g13208
21. Zhong L. Analysis of major geological disasters in China. Chinese Journal of Geological Hazard and Control, Vol. 10, No. 3, 1999, pp. 1–10.
22. Zhang S., Zhang L. Assessment of Human Risks Posed by Deadly Debris Flow in the Wen-chuan Earthquake Area. International Journal of GEOMATE, 8(1) 2015, pp.1207–1211. https://doi.org/10.21660/2015.15.4381